Beamline Studies for the PIENU Experiment

by

Rohan Nuttall

A THESIS SUBMITTED IN PARTIAL FULFILLMENT
OF THE REQUIREMENTS FOR THE DEGREE OF

Bachelor of Science (Hons.)

in

THE FACULTY OF SCIENCE
(Department of Physics and Astronomy)

The University of British Columbia
(Vancouver)

April 2018

Abstract

The Standard Model of particle physics is a theory that describes how the fundamental constituents of the universe interact. Though it remains the most accurate description of the subatomic world to date, it leaves many phenomena, such as dark matter, a full theory of gravitation, and neutrino oscillations, unexplained. This incompleteness provides an opportunity for new physics to be uncovered, creating an open channel to advance our understanding of nature. The PIENU experiment aims to contribute to this effort by testing the Standard Model predicted theory of lepton university to the highest level of precision to date. This thesis details a small contribution to the analysis required to reduce some of the systematic uncertainties present in the data, so as to ensure the desired level of precision will be achieved.

Table of Contents

List of Tables

List of Figures

Acknowledgments

I would like to express my gratitude to the PIENU collaboration for the opportunity to gain exposure a vastly complex research effort. It's been a humbling and inspiring experience. Thank you to my supervisors Doug Bryman and Toshio Numao for their kindness, inviting me to the group and defining an interesting project for me to work on. Thank you to Tristan Sullivan for his willingness early on in explaining many of the details I had difficulty grasping. Thank you to Saul Cuen-Rochin for his previous analysis that formed the essential basis for this work, and his approachability and patience to help me grasp and build upon it.

Chapter 1

Introduction

1.1 Background theory

1.1.1 The Standard Model

There are two types of particles in the Standard Model (SM): fermions, which are half-integer spin particles, and bosons, which are integer-spin particles. Bosons are responsible for carrying the forces experienced by fermions, which in the SM are limited to the electroweak and strong force. The electroweak force occurs through the exchange of photons, $W^{\pm}$ (charged-current), and Z bosons (neutral current), while the strong force through the exchange of gluons. Fermions are classified as either quarks (which experience the strong and electroweak force) or leptons (which experience the electroweak force). There are three generations of fermions, each of which differ only in their mass [2], as shown in Figure 1.1. Lastly, there are six 'flavours' for fermions and quarks. Flavour refers to the 'species' of an elementary particle, and is parametrized by flavour quantum numbers. In the case of quarks, there are distinct flavour quantum numbers corresponding to six distinct flavours: up, down, charm, strange, top, bottom.

1.1.2 The weak interaction

Interactions between fermions occur upon exchange of a boson. The strength of an interaction is given by its respective, experimentally determined coupling constant, α, and varies widely between the electromagnetic ($\alpha_e \approx 10^{-3}$), strong ($\alpha_s \approx 1$) and weak ($\alpha_w \approx 10^{-1}$)

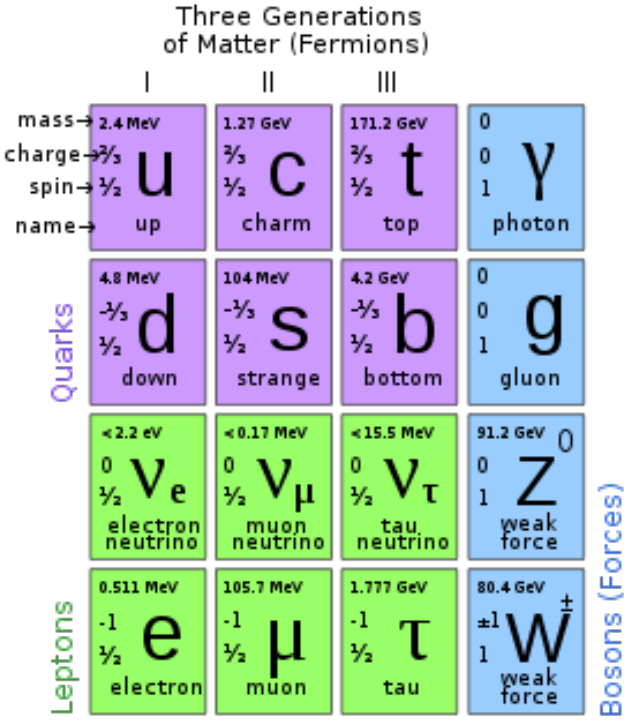

Figure 1.1: A table describing the properties of the three generations of fermions (purple and green) and the four bosons (blue) included in the Standard Model. The first generation of leptons contains the familiar electron. [1]

forces. The coupling constant for the weak force can be expressed in terms of the Fermi coupling constant, G_F, by

$$G_F = \frac{\alpha_w^2}{4\sqrt{2}M_W^2}, \tag{1.1}$$

where M_W is the mass of the W boson.

In particular, the weak interaction exhibits unique properties in comparison to the other fundamental forces, one of which being that it does not require flavour to be conserved. Conservation of flavour requires that the number of quarks and leptons be the same across initial and final states for a given interaction. While in the strong and electromagnetic interactions flavour conservation is required, the weak interaction is capable of changing the flavour of quarks. One such interaction that is permitted through this property is the pion decay.

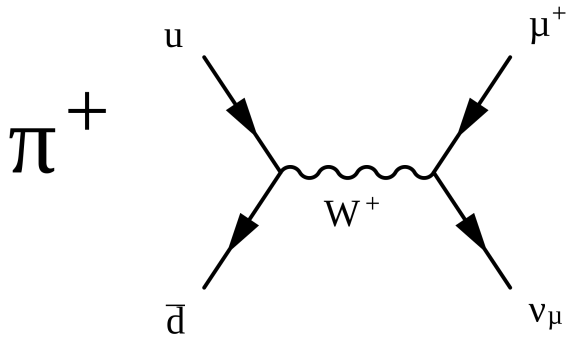

Figure 1.2: The first order Feynman diagram for a pion (π^+), composed of an up quark (u) and an anti-down quark ($\bar{d}$), decaying via exchange of a W^+ boson, to a muon (μ^+) and its respective muon neutrino (ν_μ).

1.1.3 Pion decay

Pions are a type of subatomic particle composed of a quark and an anti-quark (known as mesons) of the first generation. There are three types of pions with properties listed in Table 1.1, all of which are unstable. Charged pions decay into electrons or muons and their associated neutrinos as shown in Figure 1.2, by exchanging a $W^{\pm}$ boson.

Charge	Symbol	Composition	Mean Lifetime [ns]	Mass [MeV/c^2]
Neutral	π^0	$u\bar{u}$ or $d\bar{d}$	8.4×10^{-8}	134.9766(6)
Positive	π^+	$u\bar{d}$	26.033	139.57018(35)
Negative	π^-	$d\bar{u}$	26.033	139.57018(35)

Table 1.1: Types of pions and their properties. [3]

It might be expected that the probabilities for the decays $\pi^+ \to e^+\nu_e$ and $\pi^+ \to \mu^+\nu_\mu$ might be relatively similar. However, due to the chiral structure of the weak interaction, it is found that 99.998% of charged pions decay by the $\pi^+ \to \mu^+\nu_\mu$ mode. The mathematical structure of the weak interaction is such that it couples only to left-handed chiral particle states and right-handed chiral antiparticle states (where the projection of the spin onto the direction of momentum, or helicity, is used to define 'handedness'). Neutrinos, being effectively massless, are equivalent to helicity states. Therefore, the neutrino must be produced in a right-handed helicity state (spin projected in the same direction as momen-

tum). The pion is spin-0, so the lepton and neutrino must have spins in opposite directions. As the neutrino is fixed to be right-handed, conservation of angular momentum requires that the lepton is also produced in a right-handed state, which would be the wrong helicity for the weak interaction. However, because the helicity state can be decomposed into right and left-handed chiral states, the left-handed chiral component will still contribute to the interaction. This component is proportional to $(1 - p_l/(E_l + m_l))$, where l is the lepton in question. Therefore, highly relativistic electrons will have a very suppressed decay rate [2].

The ratio between the decay rate to electrons and muons, known as the pion branching ratio, is given by

$$R_\pi = \frac{\Gamma(\pi^+ \to e^+ \nu_e + \pi^+ \to e^+ \nu_e \gamma)}{\Gamma(\pi^+ \to \mu^+ \nu_\mu + \pi^+ \to \mu^+ \nu_\mu \gamma)}, \tag{1.2}$$

where the terms with γ correspond to the radiative decay modes where a photon is emitted. Theoretical calculations give an extremely precise value of $R_\pi^{SM} = (1.2352 \pm 0.0002) \times 10^{-4}$. This, along with the fact that R_π is experimentally accessible to accurately measure, makes the branching ratio a highly sensitive probe of the nature of the weak interaction's relationship with the electron and muon [4].

1.1.4 Lepton universality

It is predicted by the Standard Model that the coupling constant for interactions between the weak force and electrons, muons or tau leptons is the same. This is known as lepton universality. However, the question of how *universal* lepton universality actually is will have dramatic implications for our understanding of new physics beyond the Standard Model [5].

While the exact calculations for R_π are irrelevant for the theoretical scope of this thesis, the following expression for the decay rate provides important information about its dependence on the weak coupling constant [6],

$$\Gamma_{\pi \to l} = \frac{G_F^2 V_{ud}^2 m_\pi F_\pi^2 m_l^2}{4\pi} \left(1 - \frac{m_l^2}{m_\pi^2}\right) \tag{1.3}$$

where l is a lepton, V_{ud} is the upper diagonal element of the Cabbibo-Kobayashi-Maskawa (CKM) matrix, m_π is the mass of the pion, m_l is the mass of the lepton, and

F_π is a constant accounting for strong interaction effects (which cancels in Equation 1.3. From Equation 1.3 and 1.1, it can be seen that rate of pion decay to either electrons or muons is proportional to α_w^4. Indeed, if the couplings of the W boson to electrons and muons are not the same, R_π becomes:

$$R_\pi = \left(\frac{\alpha_w^e}{\alpha_w^\mu}\right)^2 R_\pi^{SM}. \tag{1.4}$$

The measurement of R_π is extremely sensitive to a presence of pseudo-scalar couplings (due to the lack of helicity suppression in such interactions), which arise in many extensions of the Standard Model, such as those with charged Higgs particles, lepto-quarks and SUSY particles [7].

1.2 The PIENU Experiment

The PIENU experiment aims to make the world's highest precision measurement of R_π for the two leptonic decay modes $\pi^+ \to e^+\nu_e$ and $\pi^+ \to \mu^+\nu_\mu$. Since the 1960s, efforts have been made to measure this branching ratio. The latest average from the Particle Data Group reported a precision of 0.33% [8], compared with the theoretical precision of $< 0.01\%$. In 2015, the PIENU Group achieved 0.24% precision with $R_\pi = (1.2344 \pm 0.0023$ (stat) ± 0.0019 (syst)$)\times 10^4$ [7]. The end goal of the PIENU experiment is to achieve $< 0.1\%$ precision, corresponding to $< 0.05\%$ precision on the ratio of the leptonic coupling constants in Equation 1.4.

1.2.1 Experimental technique

The fundamental technique behind measuring the branching ratio involves stopping a pion beam in scintillator target and counting the decay positrons from the $\pi^+ \to e^+\nu_e$ and $\pi^+ \to \mu^+\nu_\mu$ decays in a calorimeter, as drawn in Figure 1.3. The decay positrons from the former, being a two-body decay, have a well-defined energy spectrum peaked at 69.8 MeV.

However, the latter involves a three body decay, from the muon decay, $\mu^+ \to e^+\nu_e\bar{\nu}_\mu$. This results in the final positron's energy being distributed between its rest energy, 0.511 MeV, and half the muon mass, 52.8 MeV. The two overlapping energy distributions, as seen

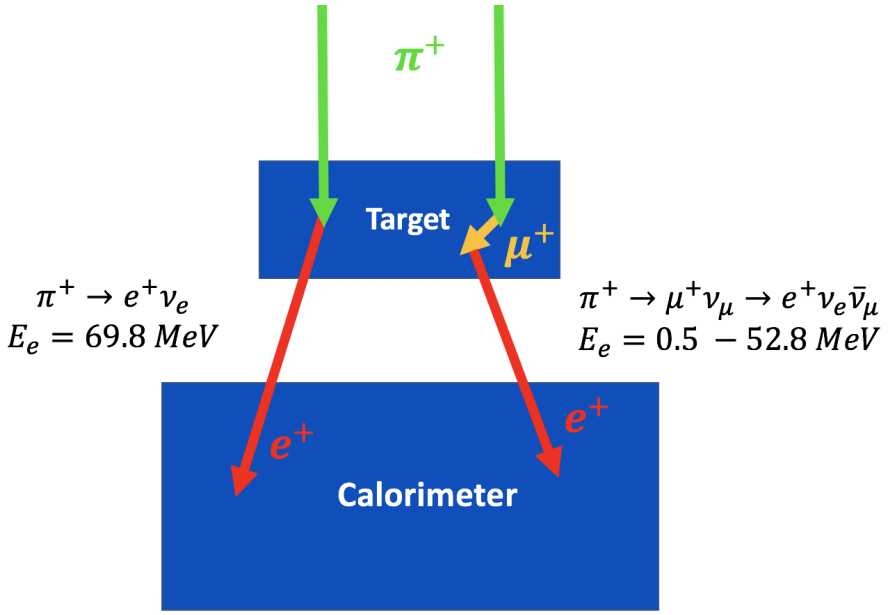

Figure 1.3: A simplified diagram of the experimental technique. Incoming pions (marked in green) stop in the Target, where they either decay directly to a positron (with a well defined energy of 69.8 MeV) by the $\pi^+ \rightarrow e^+\nu_e$ channel, or to a muon and then a positron (with an energy between 0.5 - 52.8 MeV) by the $\mu^+ \rightarrow e^+\nu_e\bar{\nu}_\mu$ channel. The energies of the final decay positrons are measured in the Calorimeter.

separated by Monte Carlo simulation in Figure 1.4, requires that events are separated into high and low energy regions in order to calculate R_π. The cutoff, E_{cut}, for the low energy region is chosen to be 52 MeV.

In order to count the decay positions, the PIENU detector comprises several wire chambers and silicon strip detectors for particle tracking, plastic scintillators for timing information and particle identification, and a crystal calorimeter array to provide the energy measurement. The main energy measurement device is a cylindrical NaI(TI) crystal, which was surrounded by 97 CsI crystals. Figure 1.5 shows the spectrum of the combined energy response for the detector. The dotted line around 52 MeV marks the point where the low energy tail from the $\pi \rightarrow \mu \rightarrow e$ interferes with the $\pi \rightarrow e$ energy spectrum. Effectively separating events from these two decays is critical for reaching the precision goal of the experiment. While there are many types of events that could cause triggers in the detector, most of this background could be removed by applying selection cuts. One of the sources

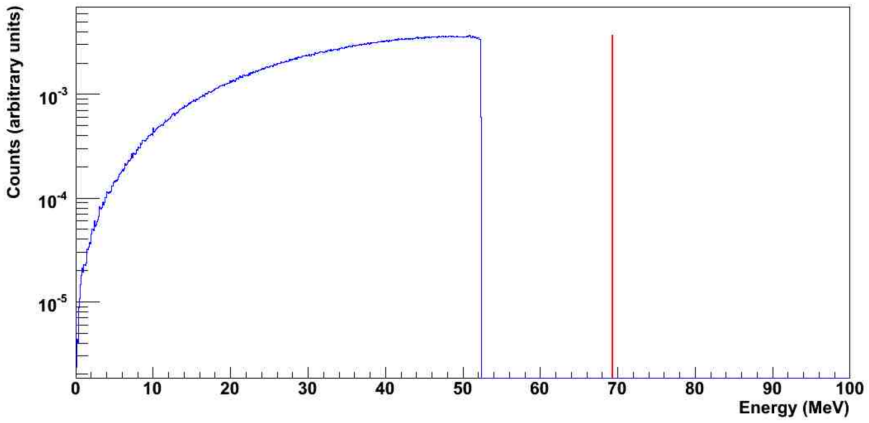

Figure 1.4: A Monte Carlo simulation of the starting energies of positrons for the $\pi^+ \to e^+ \nu_e$ channel (red) and $\mu^+ \to e^+ \nu_e \bar{\nu}_\mu$ channel (blue) [6].

of background came from the beamline itself, which delivered a beam to the detector comprising roughly 85% pions, 14% muons and 1% positrons. While the most important events to characterize were ones resulting in a high energy deposit in the crystal calorimeters (as they could be mistaken for $\pi^+ \to e^+ \nu_e$ events), there was also interest to properly characterize the low momentum tail distribution signal.

1.3 Motivation for beamline studies

The largest correction to the branching ratio comes from the proportion of $\pi^+ \to e^+ \nu_e$ events that fall below E_{cut}. These low momentum events arise from the response function of the crystal calorimeters due to photon leakage from the edges of the calorimeters, as well as radiative decays [9] (Figure 1.6). The size of this tail fraction, T, was determined to be roughly 3% [6] and is related to the branching ratio by

$$(1-T)R_\pi^{true} = R_\pi^{raw}, \tag{1.5}$$

where R_π^{raw} is the branching ratio obtained from the fits performed on the energy spectrum in Figure 1.5 before any other corrections are made. The response function of the crystal calorimeters to a 70 MeV positron beam was used, in part, to give an estimate of the low energy tail. Due to the intrinsic low energy components from scattering in the beamline itself, this empirical measurement only gave access to an upper-limit on the tail fraction. If

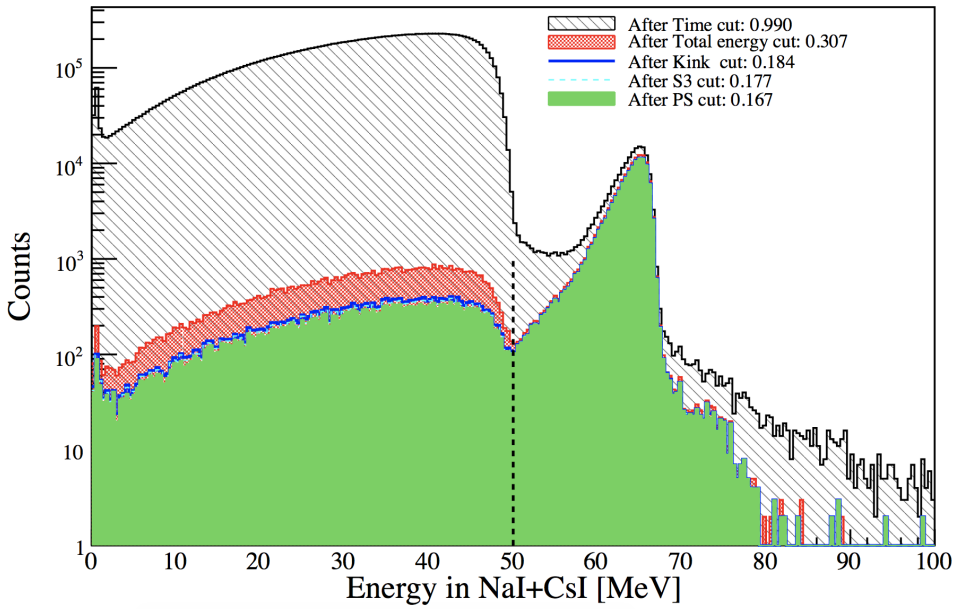

Figure 1.5: The energy spectrum including a series of background suppression cuts (shaded regions). The dotted vertical line indicates the boundary below which events contribute to the low energy region [9].

ΔT is the uncertainty on T, then the corresponding uncertainty on the true branching ratio is $\frac{\Delta T}{1-T} \cdot R_\pi^{true}$, therefore ΔT must be much less than 0.1% to satisfy $\frac{\Delta R_\pi}{R_\pi} < 0.1\%$.

One contribution to the systematic uncertainty in ΔT itself is the quantity of low momentum positrons present in the beamline. Therefore, there is a need to study and quantify the intrinsic positron momentum tail distribution from the beamline to understand more about the PIENU tail distribution signal. This is achieved by simulating the production of the beam, transport through all beamline components and energy dissipation in the final detector using a combination of software packages.

A special set of experimental positron runs used to calculate the tail upper limit in 2011, known as the lineshape measurement. In 2012, one week of beamline tests were performed. Part of this datataking involved tuning various settings along the beamline (discussed in Chapter 2.2), and served as a set of run data to validate the accuracy of the simulations performed to determine the instrinsic tail from the positron beam. This is the point of departure for the work described in this thesis.

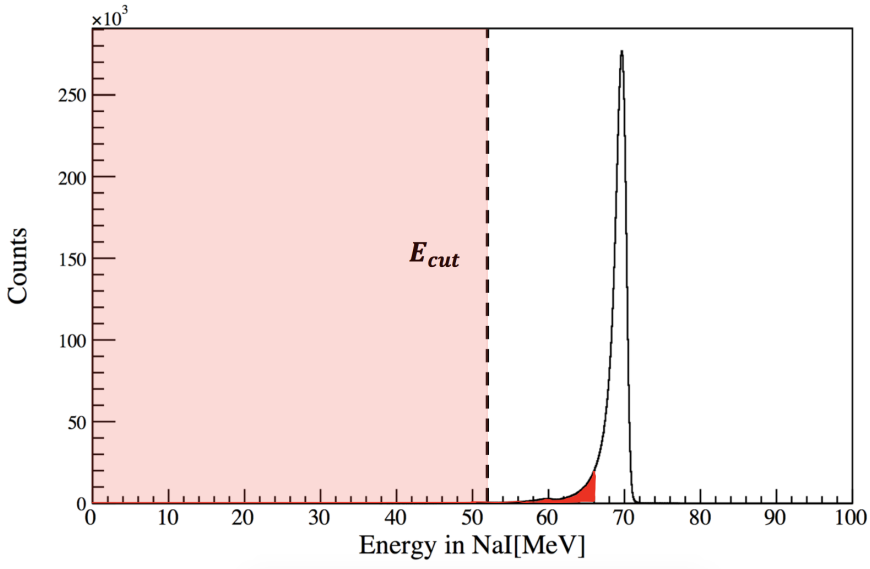

Figure 1.6: The energy response from the NaI calorimeter. The 'tail' that appears below 70 MeV is filled in red for illustrative purposes. The shaded region corresponds to the region of low energy events, marked by E_{cut} = 52 MeV. The motivation of the beamline studies is to determine the proportion of low energy events that fall in this region.

Chapter 2

Simulation

2.1 G4Beamline

In order to determine the intrinsic positron momentum tail from the M13 beamline, it is necessary to be able to track the position and momentum of particles as they traverse the beamline. `G4beamline` is a particle tracking and simulation program based on the `Geant4` toolkit [10]. Intuitive commands that wrap more complex C++ code makes the task of importing the real beamline into the program straightforward. In this way, all of the sophisticated simulation machinery implemented in `Geant4` can be exploited without having to directly use it.

The input file for the simulation is written in a single ASCII file. `G4beamline` permits the user to define an arbitrary list of settings, materials, geometry and specific beamline elements, such as bending magnets and quadropoles, as objects. Parameters can then be declared globally to store specific settings for the objects and allow for single point of control, which is essential for complex or large input files. After this is done, the next task is to place the objects along the direction of the beamline. This can be done in one of two ways, either using global coordinates or centerline coordinates. The former requires X, Y, and Z coordinates to specified for the placement of each element, while the latter represents the nominal center of the beamline. This allows for all objects to be placed by simply specifying their distance (along Z) downstream of the beam production target.

G4beamline includes simple geometric elements such as tubes and boxes which can be used to model beam pipes, walls and slits. It also has a list of more complicated elements such as *genericbend* and *genericquad* which define the geometry and field details for individual magnets. As the simulation aims to replicate reality as accurately as possible, the parameters for these objects must be tuned to achieve various desired characteristics found in the real beamline. Several of these parameters and an estimation of their uncertainties is presented in Section 2.2.

The output of the simulation is obtained by using the *virtualdetector* command to generate an NTuple that contains information for all tracks that pass through it. An NTuple is a commonly used datatype implemented in ROOT that consists of a tabular, fixed length row of data, where each element in that row of data is restricted to a floating point value corresponding to a particular variable (i.e. momentum along x, position along y, time of hit, particle ID). The material of the virtual detectors are chosen to be 'vacuum' such that they simply measure all the track properties without interfering with the particle itself. Upon compilation, G4beamline writes all of the recorded hits into a ROOT output file.

In order to analyze the output, it was possible to use the add-on program HistoRoot, which provides a user-friendly way of generating and plotting from .root files via a graphical user interface [11]. However, in order to avoid potential limitations, several ROOT macros were written (included in Appendix A) to allow for more flexibility in the kinds of analysis to be done.

2.2 Beamline: geometry and settings

The M13 beamline is a low energy muon and pion beamline [9]. The beam channel begins after the beryllium production target (labeled T1 in Figure 2.1), which receives a 500 MeV proton beam with an intensity of 120 μA from the main cyclotron. A series of quadropole and bending magnets focus and steer the beam through a series of background suppressing installations.

After the production target, the beam passes through a pair of quadropoles (Q1-2) and a horizontal slit and vertical jaw (F0SL, F0JA) to define an acceptance window of the beam.

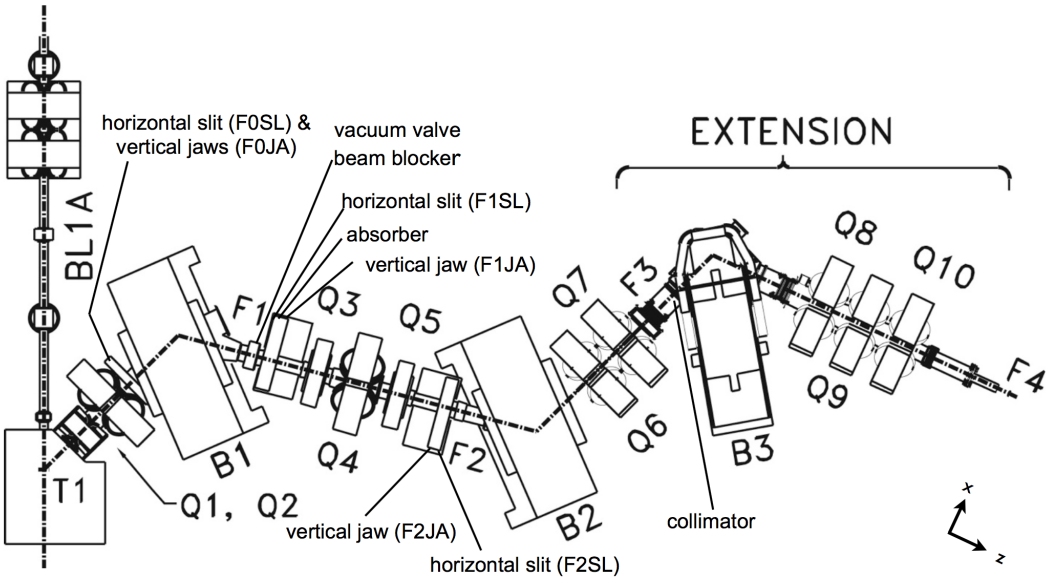

Figure 2.1: Schematic of the M13 beamline.

The first bending magnet (B1) steers the beam into focus point 1 (F1), where it encounters a momentum-defining slit-jaw (F1SL/F1JA) and lucite absorber (to cause momentum spread between positrons and pions) are located. A triplet of quadropole magnets (Q3-5) work to focus the beam before the second momentum-defining slit-jaw (F2SL/F2JA). A second bending magnet (B2) steers the beam through two more quadropoles (Q6-7) before passing through a lead/brick collimator that serves to stop the positrons displaced by the absorber and further clean up the beam. The quadropoles work in pairs or triplets to ensure there's no divergence along the x and y axis. A final bending magnet (B3) steers the beam towards the PIENU detector. The beam is refocussed by the last three quadropoles (Q8, Q9, and Q10), and passes through a steel wall to provide shielding from γ-rays emitted from stopped positrons in the collimator. After the steel wall, the beampipe radius is reduced from 15.5 cm to 9.8 cm until it ends at the last focus point (F4) and enters the detector.

For the 2012 positron runs, the bending magnets were tuned to select positrons instead of pions. Furthermore, the absorber and collimator weren't included in the configuration.

The production target was implemented using the *beam* object in `G4beamline`, which provides various options for beam distributions. This consisted of injecting a positron beam

with a Gaussian spread in momentum and position space. The value for momentum spread was nominally taken to be $\sigma_p = 0.7$ MeV, such that 99.7% of the positrons has a momentum within 3% of 70 MeV [12]. For all of the studies, the beamline geometries and settings were obtained from the Experimental Physics and Industrial Control System (EPICS) logs and are listed in Tables 2.1 and 2.2. EPICS software systems are commonly used as distributed control systems for particle physics experiments. They collect experiment and control data in real-time and allow for a client to access a full history of run settings. This extensive dataset is stored in a large spreadsheet (`.ODS` file format) for each run. Appendix A includes the script used to parse these files in order to extract the relevant lines for the specific beamline settings of interest to these studies.

Name	Value
Positron beam mean momentum	70 MeV
Momentum spread	$\sigma_p = 0.7$ MeV
Beam spot size (Gaussian shape)	$\sigma_x = 3.656$ mm, $\sigma_y = 3.133$ mm, $\sigma_x = 1.833$ mm
B1 field	0.2077061 T
B2 field	0.2077061 T
B3 field	0.2630311 T
F0SL width	120.2 mm
F1SL width	15.5 mm
F2SL width	30.4 mm

Table 2.1: Some parameters used in the model of the production target, bending magnet strengths, and slit positions for the nominal setting.

Name	Value [mm]
Q1	103.2
Q2	155.6
Q3	101.6
Q4	155.6
Q5	101.6
Q6	155.6
Q7	155.6
Q8	155.6
Q9	155.6
Q10	155.6

Table 2.2: Apertures of the ten quadropole magnets used in the G4beamline simulation.

2.3 Current Focus

2.3.1 Previous work

In an effort to track the origin of the intrinsic low momentum tail from the beamline at F4, Saul Cuen determined that [13]:

- the tail arises due to scattering in different beamline components
- the positron energy tail in Bina+CsI is between 0.1% and 0.2%

The second point was achieved by loading the distribution of positrons, γ-rays and electrons at F4 into the PIENU Geant4 code to obtain the final tail fraction. However, several concerns around the validity of the simulation were raised upon comparison with 2012 data for the beamline tests. While the simulation agreed well with results for dipole magnet tunings within the $\pm$5% range, the simulation seemed to show that the beam was exiting the pipe for higher magnet field settings for B3. Despite their effectiveness at modelling physical systems, Monte Carlo simulations are not invulnerable to errors and unphysical behaviour. As more pressing studies were underway at the time of Saul's studies, this particular work was put on hold. Without further investigation to confirm whether the observed behaviour was physical or unphysical, the confidence in the `G4beamline` simulations for determining the tail fraction was put into question.

This project aims to perform these further investigations in order improve confidence in the validity of the simulation. Chapter 3 re-examines previous work done by Saul and extends the study to include systematic tests and more run comparisons with different B3 tunings.

2.3.2 Simulation systematics

An attempt was made to investigate the influence of several other starting distributions of particles on the results at the end of the beamline. The outcome of these studies is discussed in Chapter 3.2.4. Furthermore, the two main aspects that influence the accuracy of the simulation include how closely the geometry of the simulation matches the real geometry and how accurately the real electromagnetic fields are modeled in the simulation. The extent to which the uncertainty in the magnet current values and the location of certain beamline components affect the results of the simulation at the end of the beamline are briefly addressed in Chapter 4.

Chapter 3

Results

3.1 Simulation uncertainty

The statistical uncertainty of the tracked particles along the beamline is governed by the number of events generated. As the main goal of this work is to study various systematic parameters and configurations of the simulation to improve the confidence on the beamline momentum tail value, it was important to be able to analyze the results from each run before adapting the input file and running another test. Therefore, enough events had to be run to produce statistically meaningful results while also ensuring the CPU time was not too long.

In order to get a relative uncertainty of, say 0.1%, it may seem reasonable to claim that starting with 10^6 events would be sufficient. However, in the case of the M13 beamline, roughly 1% of the total histories generated at the start of the beamline survive to the end (due to loss processes such as multiple scattering and ionization). To meet a 0.1% uncertainty in the tail fraction calculation, at least 10^8 events would need to be run for each simulation, taking just over 60 hours. As shown in Figure 3.1, dramatic increases in computation time would be expected beyond 10^8 primary events. Clearly, trade-offs between CPU time and simulation uncertainty must be made.

3.1.1 Determining optimal number of histories

In order to obtain a better understanding of the point at which the simulation stabilizes, simulations were run with primary events ranging from 10^3 - 10^8 particles and the tail

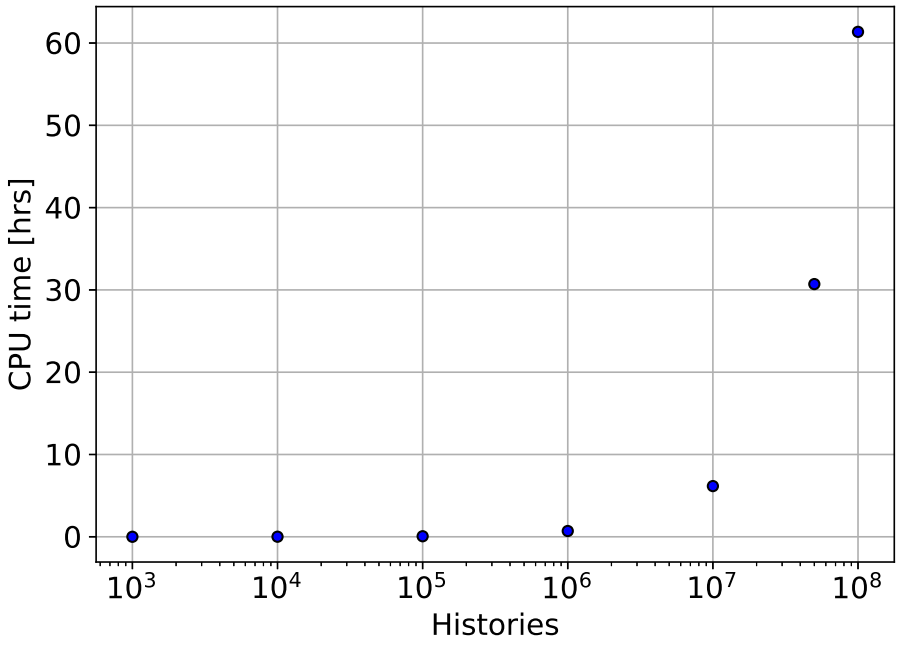

Figure 3.1: Computation time on the PIENU local cluster.

fraction was calculated. The statistical uncertainty on the tail fraction was determined by the quadrature sum

$$\delta T = \sqrt{\left(\frac{\delta N_{LE}}{N_{LE}}\right)^2 + \left(\frac{\delta N}{N}\right)^2} \cdot T, \tag{3.1}$$

where N_{LE} is the number of low energy positrons (with momentum less than 52 MeV), N is the total number of positrons, and T is the tail fraction at the end of the beamline. Figure 3.2 reports the statistical error on the simulated tail fraction from the beamline as a function of histories.

Essentially, the task is to choose the number of histories that will allow for an observation of any deviations in the tail fraction due to the systematic uncertainties of the simulation, independent of the statistical uncertainty. It can be seen that for 10^7 histories, $T = 0.049 \pm 0.009$, which is less than the 0.1% cutoff required for the precision of the experiment while requiring less than 10 hours on the PIENU local grid to run. Hence, this number of histories can be used with confidence to study the effect of the various systematics influencing the accuracy of the simulation.

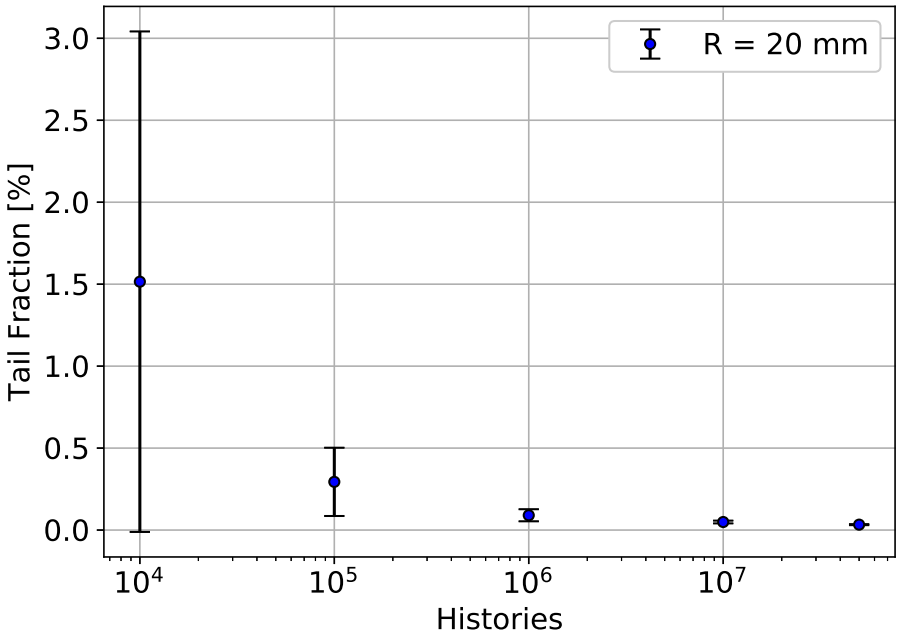

Figure 3.2: The calculated tail fraction and statistical error for a range of histories. As expected, the statistical uncertainty decreases with increasing number of starting events. It should be noted. The acceptance cut is 20 mm, meaning that only events within 20 mm in x and y are included in the tail fraction calculation. As this cut is relaxed, the tail fraction inevitably increases. This value is chosen to be in line with previous work [13].

3.2 Simulation accuracy

How realistic the simulation is depends on the accuracy of the geometry used in the simulation, electromagnetic fields, and modeled beam distributions. This section explores the influence of these parameters on the accuracy of the results. In search of a way to quantitatively compare the effect of the simulation accuracy when various parameters are toggled, three tests are employed.

While there are numerous methods–some more statistically rigorous in their implementation than others–to determine the similarity between two distributions, the most natural way to compare the degree to which the simulation matches the experimental data is to calculate the distance between the peak heights, Δ_{peak}. This is because we *expect* that the simulation should agree with the run data, so this gives a measure of the extent to which the agreement diverges. For completeness, the `ROOT` implementation of the χ^2 test for

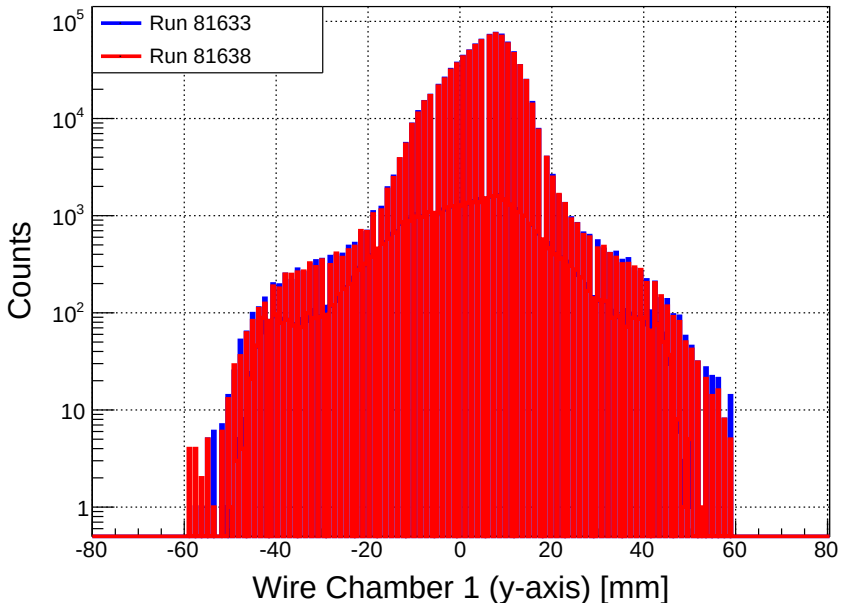

Figure 3.3: A test for the similarity between two beam position profiles (y) of run data that should be identical. Run 81633 and 81634 were both taken with nominal beamline settings. This test was done to obtain the nominal values for the statistical compatibility tests.

comparing experiment/Monte Carlo data and the Kolmogorov-Smirnov compatibility test for assessing the similarity in shape between two histograms are used. Regarding the later, though there are some limitations to this test (namely that when applied to binned data the probability of compatibility is overestimated), for the practical purposes of getting a general sense of how the simulation data behaves under variation of different parameters, it's still undeniably better than qualitative inspection 'by eye'.

In order to obtain a reference point for these tests, the y position profiles (Figure 3.3) for two of nominal experimental data were analyzed for similarity in the manner described. Though by inspection they appear almost entirely identical, the results from the statistical tests for similarity are shown in Table 3.1. The differences of the other simulations are measured relative to these values.

Δ_{peak}	χ^2	Kolmogorov Test
0.00	166.21	0.0013128

Table 3.1: Difference between the data plotted in Figure 3.3 for runs 81633 and 81634.

3.2.1 Influence of beamline components

As the statistical uncertainty on the tail fraction depends on the number of particles that survive to the end of the beamline, it was hypothesized that it could be unnecessary to simulate the entire beamline. Figure 3.4 shows a rendering of the full beamline and the normalized momentum profile at F4, while Figure 3.5 shows the momentum profile for the reduced beamline.

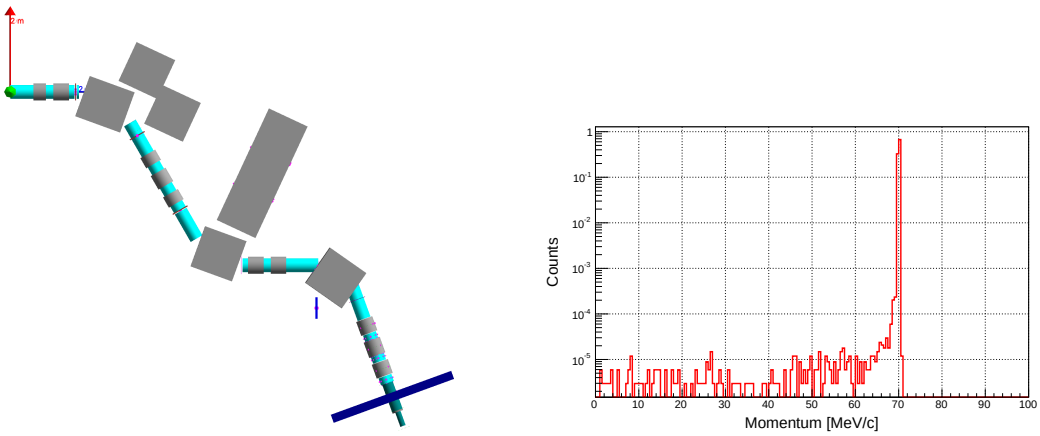

(a) **(b)**

Figure 3.4: The full 3D render of the M13 beamline is shown in (a). The light blue elements correspond to the beam pipe sections (starting at the red axis arrow), while three grey boxes along the beamline depict the bending magnets. The other grey boxes correspond to the concrete shielding boxes. The dark blue plate at the end of the beamline is the steel wall before the stainless steel piping in turquoise. Figure (b) shows the momentum profile at focus point 4, where the low momentum tail spans the entire region below 52 MeV.

While more events survive (96%) using less CPU time, the momentum profile in the reduced beamline case does not include the low momentum tail observed in the case of the full beamline. In fact, the momentum distribution is almost identical to the beam supplied at the beginning of the beamline. The reason behind why this is can be observed in Figure

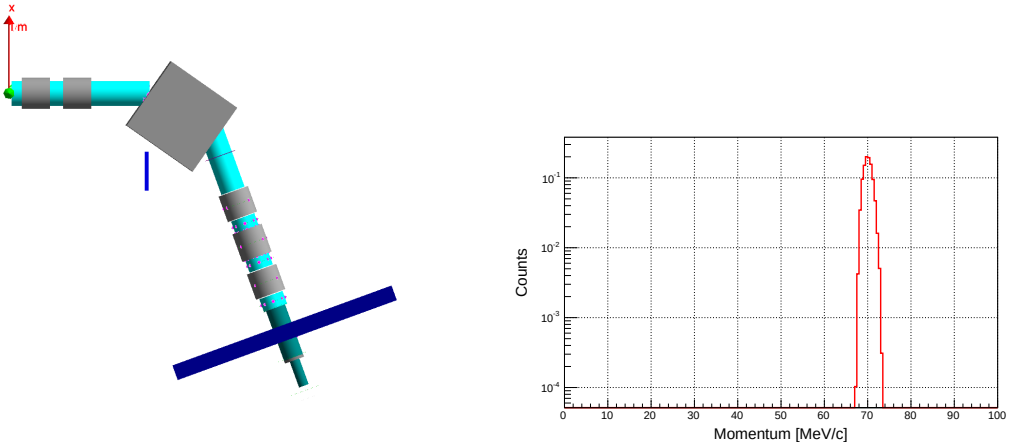

(a) **(b)**

Figure 3.5: The 3D rendering of the reduced M13 beamline is shown Figure (a), where the all components before the last beam pipe section before the third bending magnet are omitted. Firgure (b) shows the momentum profile at focus point 4. Unlike in Figure 3.4, there is no low momentum tail evident. This suggests that the tail origin is before the third bending magnet.

3.6, where a large amount of scattering occurs at the horizontal slits and vertical jaws after the first bending magnet and before the second bending magnet.

By placing a virtual detector downstream from F1, but before Q3, the spread in the beam along the x-axis and corresponding momentum distribution induced by the scattering on the slits can be visualized. In Figure 3.7, the majority of the particles pass through the slit width (which is set to 15.5 mm) while 11.7% scatter off the slit but still remain contained within the beam pipe. That is, their position is within the bound 15.5 mm $< x <$ 155.6 mm. These particles account for the significant low momentum tail in Figure 3.8. Within the radius of the beam pipe, the tail fraction is 24.9% but reduces to 9.8% if the acceptance radius is taken to be 20 mm.

To observe the evolution of the tail fraction as the beam traverses the beamline, Table 3.2 lists the tail fraction at 17 virtual detectors along the beamline. There are three locations at which the tail fraction increases considerably: after the first slit, after the second slit and between the third bending magnet and eighth quadropole magnet. While the cause of the tail fraction increase at the first two locations is due to scattering off the slits, the reason for the increase after the bending magnet is less obvious. By inspecting Figure 3.9c, it's

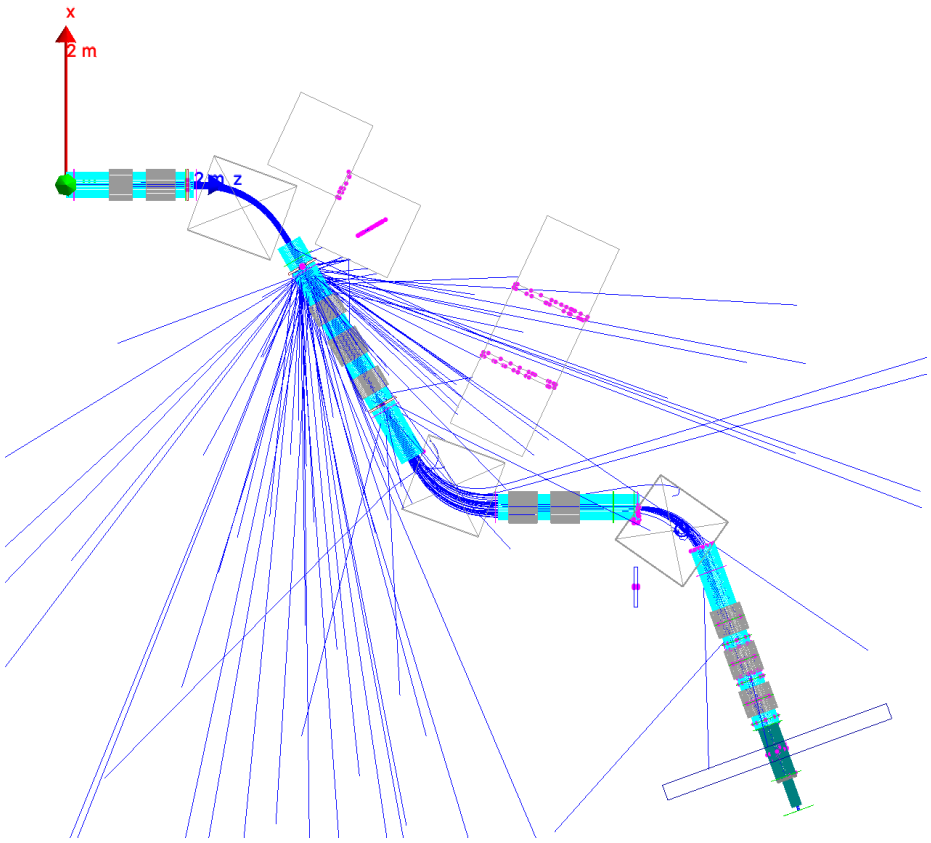

Figure 3.6: A wireframe plot of the M13 beamline with a trace of 10,000 events (dark blue trajectories) overlaid. It can be seen that a major scattering event occurs at the first focus point, while additional scattering occurs before the second and third bending magnets.

evident that the magnetic field causes some particles causes some dispersion in the beam. It's evident that there's low momentum components that make it through and that even the quadropole magnetic isn't effective at completely focusing the beam.

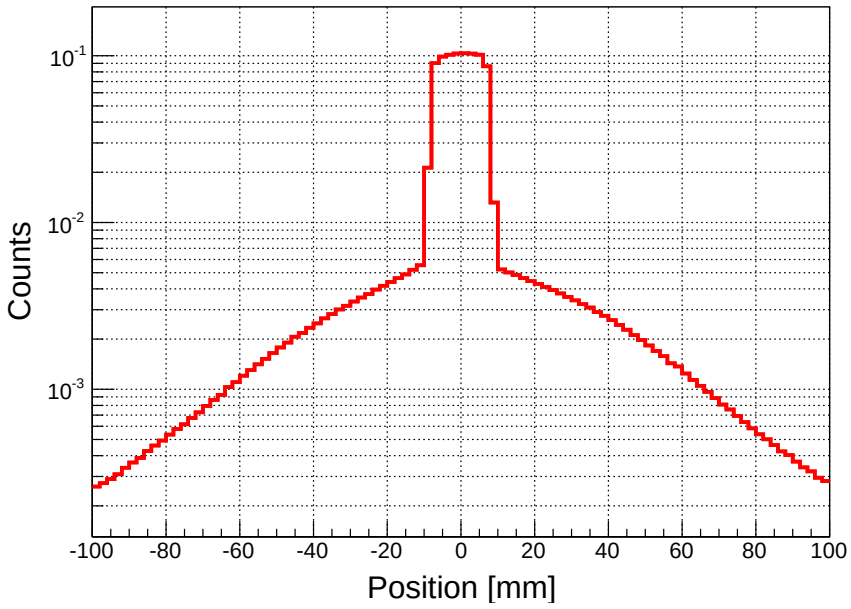

Figure 3.7: Position distribution immediately after the first slit/jaw. The trailing edges past 15.5 mm (the width setting for F1SL/F1JA) represent the scattered trajectories and are responsible for the large low momentum tail observed in Figure 3.8.

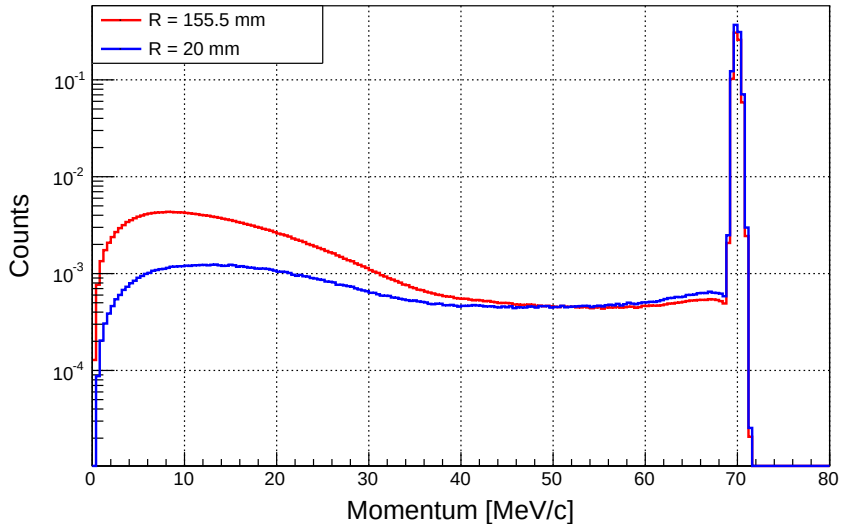

Figure 3.8: Momentum distribution immediately after Slit 1. A larger tail fraction (in red) can be observed when the acceptance cut is set to the full beam pipe radius, R = 155.5 mm.

Location	Tail Fraction [%]	Position (z) [mm]
Source	0	100.00
F0	7.22E-06	1504.79
After F0 Slit	5.91E-05	1640.69
F1	0.020	3274.19
After F1 Slit	**9.768**	3451.99
F2	0.856	5380.45
After F2 Slit	**5.502**	5473.65
After B2	0.788	7400.00
F3	0.006	9141.00
After Collimator	0.039	9193.00
After B3	**3.202**	10450.00
Q8	**4.041**	11375.43
Q9	3.182	11906.43
Q10	2.430	12439.99
Pad 1	0.18106	12517.94
After Steel Wall	0.036	12517.94
F4	0.034	13653.54

Table 3.2: The tail fraction calculated at 17 different locations along the beamline. The large increases after the F1 slit, F2 slit and B3 are marked in bold.

3.2.2 Magnetic Field at B3

How accurately the real electromagnetic fields are modeled in the simulation has an effect on ensuring the results of the simulation are accurate enough to be useful. The unexpected increase in the tail fraction between B3 and Q8 prompts an investigation as to whether or not a more accurate implementation of the magnetic field has an impact on the final results. For most of the simulations, `G4beamline`'s *genericbend* is used with the appropriate current values obtained from the EPICS log. However, it is also possible to provide the software with a *fieldmap*, which defined the electromagnetic fields from a file that's supplied. In 2007, TRIUMF's Magnet Group performed a detailed survey of the field at B3. This data was converted into the appropriate 'BLFieldMap' format required by `G4beamline`. Table 3.3 details the difference in the tail fraction and the statistical similarity of the results plotted in Figure 3.10.

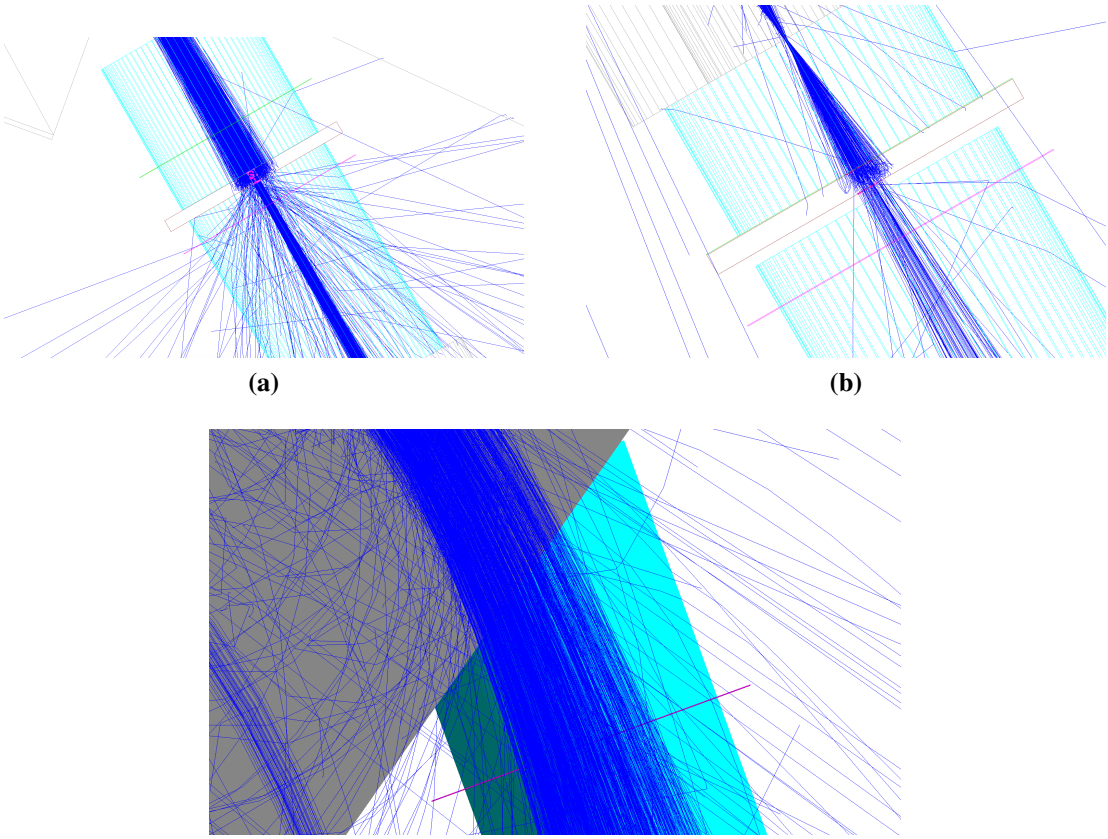

(a) **(b)**

(c)

Figure 3.9: Scattering is observed at three main locations. Figure (a) shows a close-up of the scattering event at the first slit/jaw, (b) shows scattering at the second slit/jaw and (c) shows the large number of stray trajectories whose momentum remains unfocused by B3. These events are responsible for the spike in the tail fraction observed in Table 3.2.

Simulation	Tail Fraction [%]	Error [%]	Δ_{peak} [mm]	χ^2	Kolmogorov
Generic Bend	0.0902	0.0368	8.4	90.3551	0.226386
Field Map	0.0584	0.0591	11.2	81.3912	0.369795

Table 3.3: The tail fraction and three tests for the similarity between the simulation with the *genericbend* and *fieldmap* configurations for 10^6 histories. While the tail fraction using the field map is lower, the significantly larger distance to the run data peak indicates that it isn't more effective at modeling the magnetic field implemented by *genericbend*.

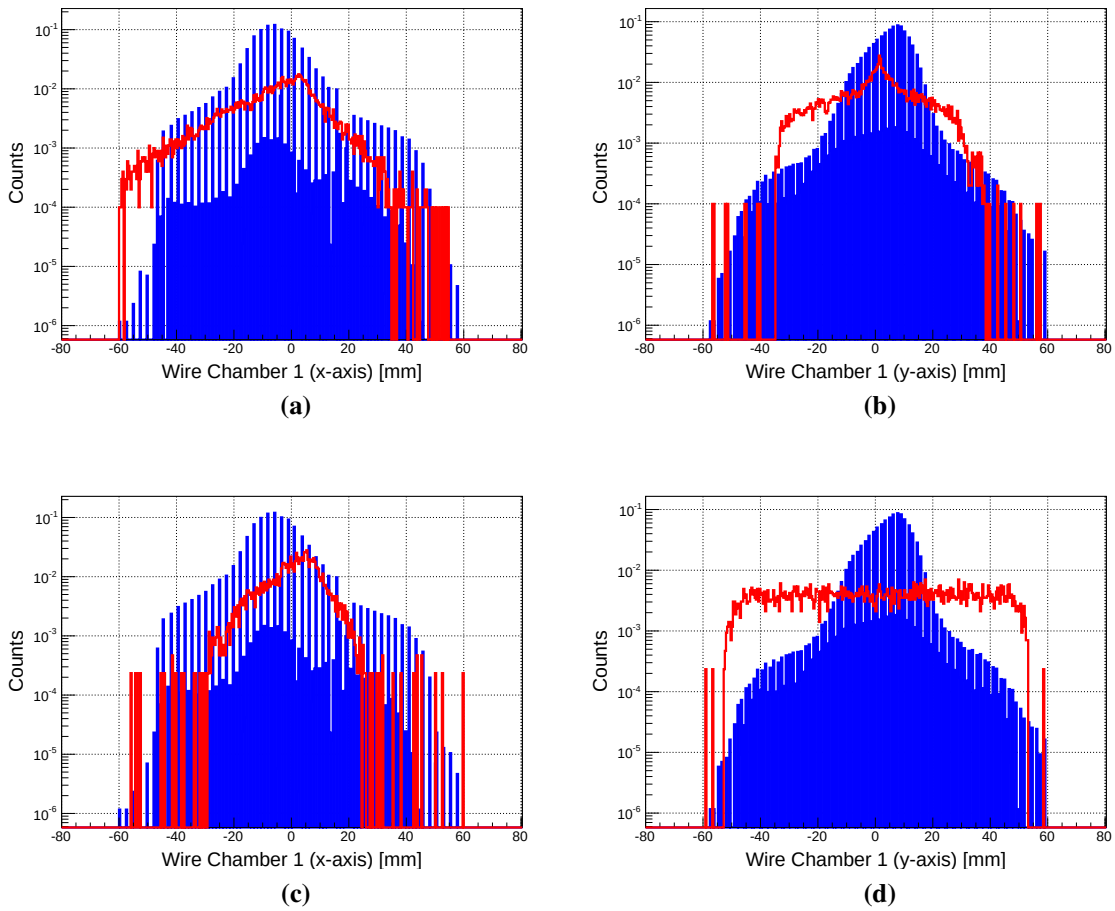

Figure 3.10: The x and y profiles for the *genericbend* (a and c, respectively) and *fieldmap* (b and d, respectively) configurations of the B3 implementation. In addition to the discrepancy in the x peaks, it can be seen in (d) that the field map also fails at replicating the y profile accurately.

3.2.3 Analyzing effect of beam distributions

In order to ensure the beamline is modeled as precisely as possible, several 'types' of beams were tested. Nine different scenarios were analyzed for both momentum and spatial deviations to determine the effect on the tail fraction, from negligible deviation to more extreme cases. How well the modeled beam distributions match the real beam will effect the accuracy of the simulations. Due to the uncertainties in the dipole magnets fringe field it is difficult to obtain an absolute beam momentum calibration, however previous studies have reported that it is well-defined to about 1% [9]. In previous studies, a percent difference

of 2% was used [12]. For completeness, Table 3.4 reports the tail fraction for select momentum spreads ranging from 0% to 50% to see the effects. The origin position sigma for momentum is chosen in each case such that 99.7% will be within the percent uncertainty, Δ_p, of the beam momentum.

Δ_p [%]	σ_p	σ_x	σ_y	σ_z	T [%]	Δ_{peak} [mm]	χ^2	Kolmogorov
0.00	0.00	0.00	0.00	0.00	0.00	6.4	0.595	0.70472
0.50	0.12	0.00	0.00	0.00	0.00012	8.8	17.297	0.49741
1.00	0.23	0.00	0.00	0.00	0.00016	8.8	2378.140	0.40910
2.00	0.46	0.00	0.00	0.00	0.00056	8.8	946.58	0.36751
10.0	2.30	0.00	0.00	0.00	0.0013	8.8	556.41	0.35237
30.0	7.00	0.00	0.00	0.00	0.00	8.8	128.744	0.35120
50.0	12.0	0.00	0.00	0.00	0.00	8.8	73.731	0.35130
2.00	**0.46**	**0.50**	**0.50**	**0.50**	**0.022**	**8.8**	**93.813**	**0.21220**
2.00	0.46	3.66	3.13	1.88	0.021	9.2	108.496	0.24147

Table 3.4: Beam distribution variations for Δ_p ranging from 0% to 50% in arbitrary increments. The last two rows vary $(\sigma_x, \sigma_y, \sigma_z)$ while maintaining the 2% deviation as in [12]. It can be seen that changing the deviation in position by 0.5 results in an order of magnitude increase in he tail fraction. This dependence could be caused from scattering within the beam pipe in the first section. The best matching starting distribution is in bold, which exhibits the lowest Komologorov statistic, a reasonable χ^2 and Δ_{peak} value. It should be noted that a more precise determination of the best starting distribution would require a finer variation of the spatial deviation.

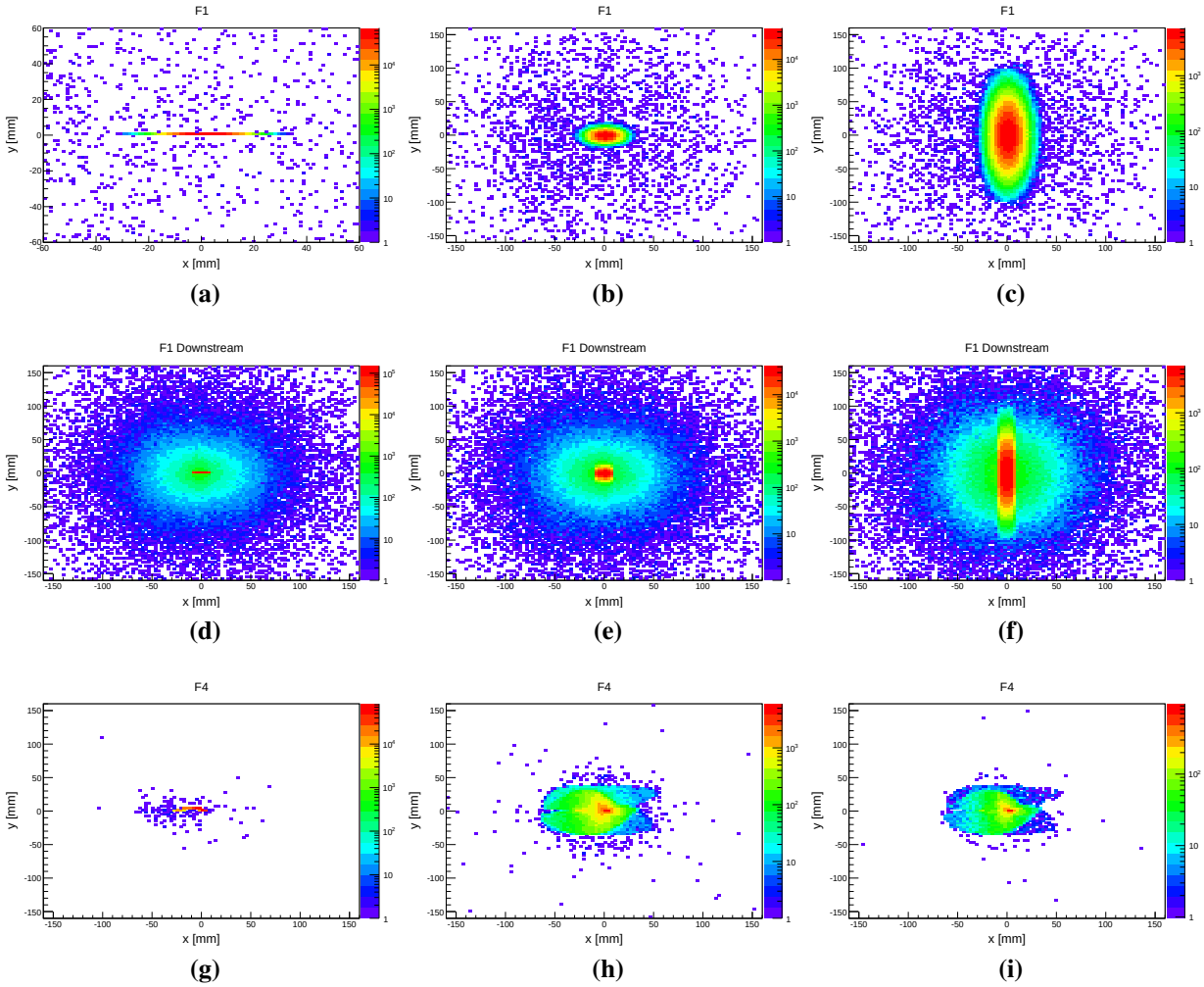

Figure 3.11: A trace of the beam spot at focus point 1 (F1), after F1, and at the end of the beamline (F4). Figures (a), (d), and (g) correspond to $\vec{\sigma}$ = (0.23 MeV, 0 mm , 0 mm, 0 mm). Figures (b), (e) , and (h) correspond to $\vec{\sigma}$ = (0.23 MeV, 0.5 mm, 0.5 mm, 0.5 mm) and figures (c), (f), (i) correspond to $\vec{\sigma}$ = (0.23 MeV, 3.66 mm, 3.13 mm, 1.88 mm). It can be seen that the divergence in the beam remains significantly lower by the end of the beamline when no deviation is applied to the position. However, for the two cases when the position deviation is varied, the similarity in the spatial distribution seems to match the similarity in the magnitude of the tail fraction. This seems to indicate that a the spatial distribution at the beginning of the beamline, to some degree, persists to the end of the beamline.

3.2.4 Effect of radially distributed beam

In order to more accurately model the beam, the beam is rotated every 10,000 events by 40°. Table 3.5 shows that this method of describing the beam has the best similarity as compared with the non-rotated beam.

Simulation	Tail Fraction [%]	Error [%]	Δ_{peak} [mm]	χ^2	Kolmogorov
Rotated	0.027	0.0049	8.32	33.9519	0.236993
Non-rotated	0.033	0.0031	8.40	90.3551	0.226386

Table 3.5: The tail fraction comparison for simulations with a rotated beam and non-rotated beam. While the two tail fractions statistically agree, the rotated beam clearly shows a better fit to the data.

3.3 B3 tuning

After establishing that the rotated beam configuration for 10^7 histories with $\vec{\sigma}$ = (0.23 MeV, 0.5 mm , 0.5 mm, 0.5 mm) is likely the best starting distribution, a comparison between the simulation and run data in Table 3.6 is made. These plots are shown in Figures 3.12 through 3.14. They appear to show good agreement across all the tunings except for the -13.3% case. While the 9.9% case is expected to be translated further in the positive x direction, by observing the 3D render in Figure 3.15, it is clear that B3 is actually steering the beam outside of the beam pipe resulting in extensive, Gaussian-like scattering. The run data collected for this tuning setting is likely also suffering from the same effect. This feature is far more extreme for the case of -13.3% tuning.

Run Number	B3 Tuning [%]
81633	0 (nominal)
81650	-3.6
81665	4.8
81657	-8.4
81670	9.9
81658	-13.3

Table 3.6: A list of runs and their corresponding tuning percentage for B3.

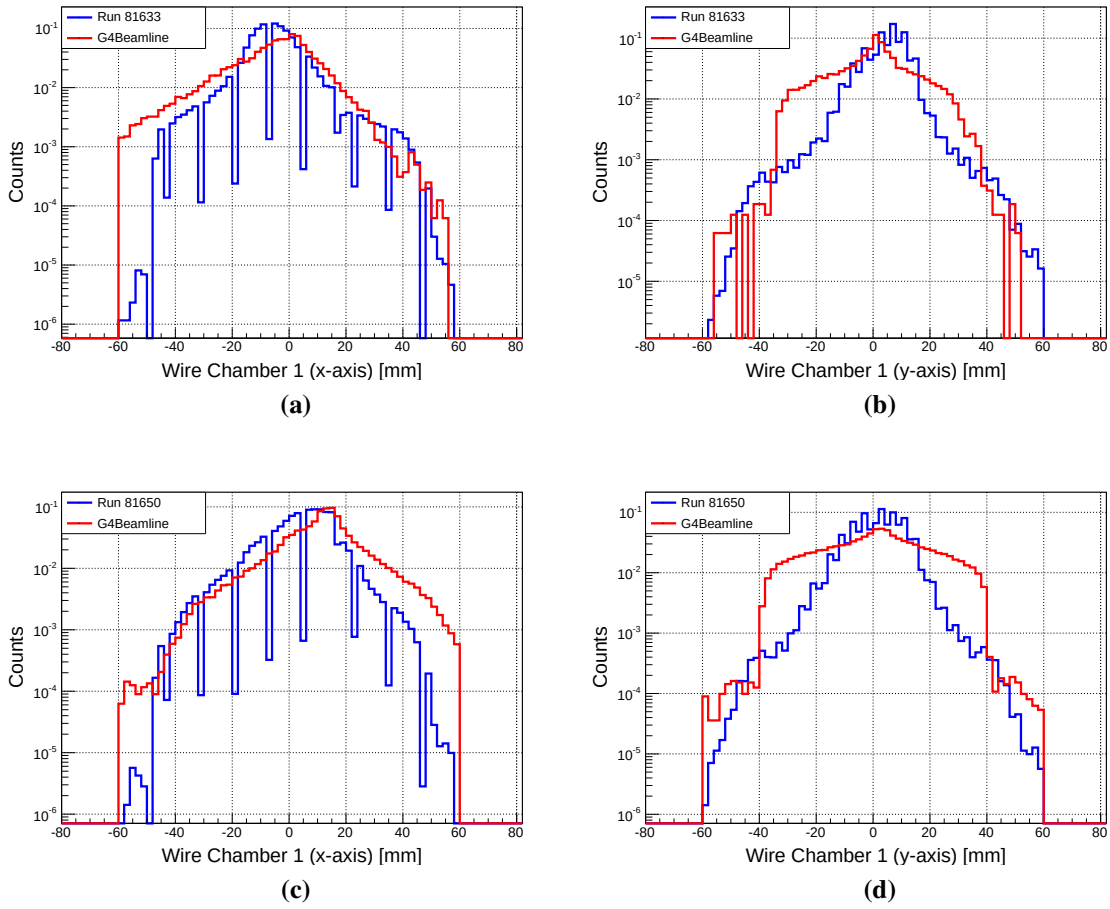

Figure 3.12: G4beamline and 2012 run data comparisons. Figures (a) and (b) correspond to nominal settings for x and y respectively, while figures (c) and (d) correspond to -3.6% tuning. The y profile does not change measurably between the two simulations, as expected. The x profile for the -3.6% tuning data follows the run data well.

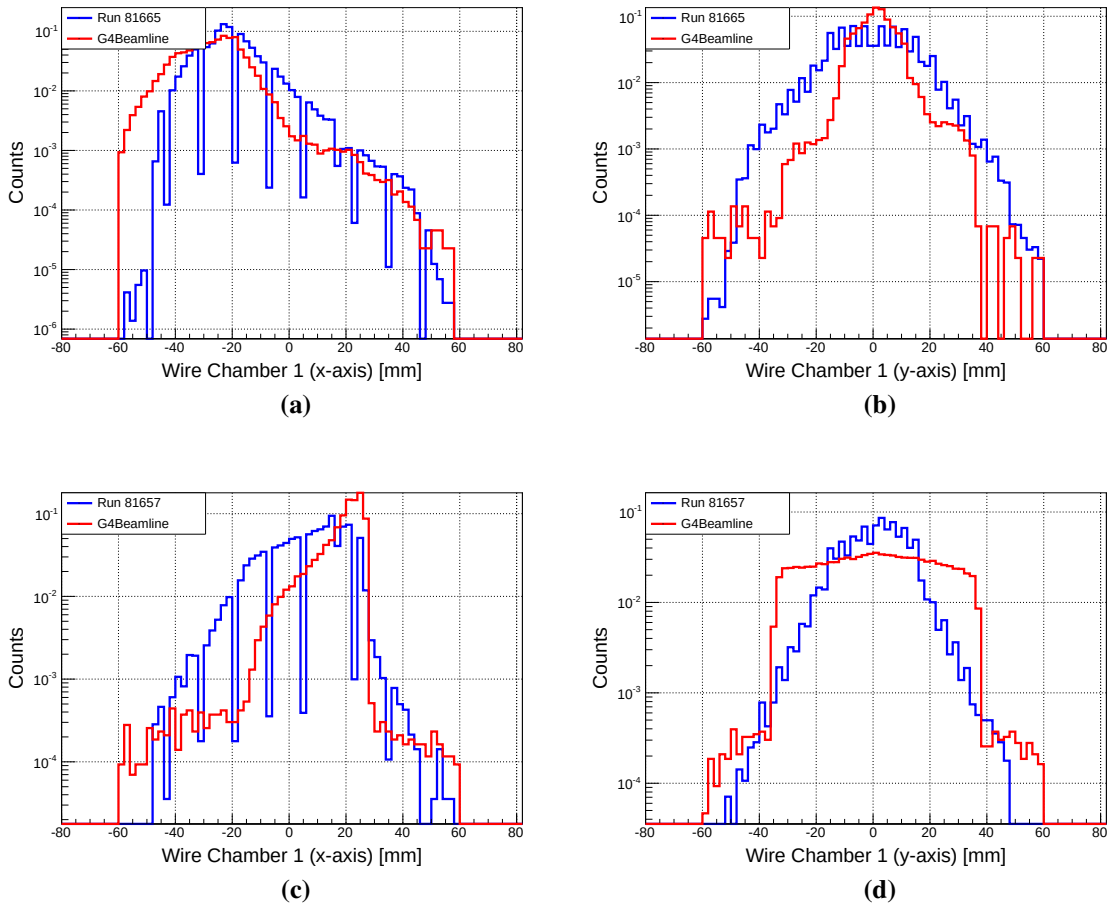

Figure 3.13: G4beamline and 2012 run data comparisons. Figures (a) and (b) correspond to +4.8% tuning settings for x and y respectively, while figures (c) and (d) correspond to -8.4% tuning.

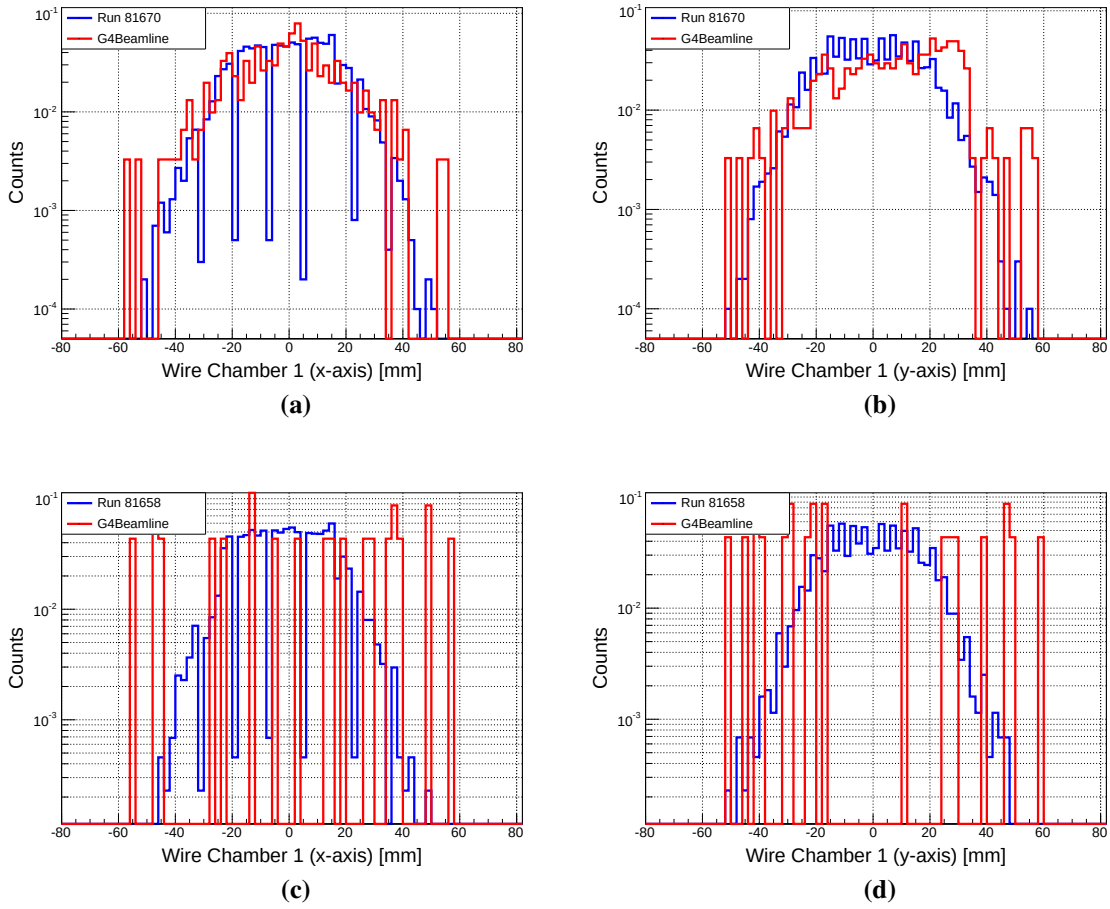

Figure 3.14: G4beamline and 2012 run data comparisons. Figures (a) and (b) correspond to +9.9%tuning settings for x and y respectively, while figures (c) and (d) correspond to -13.3% tuning.

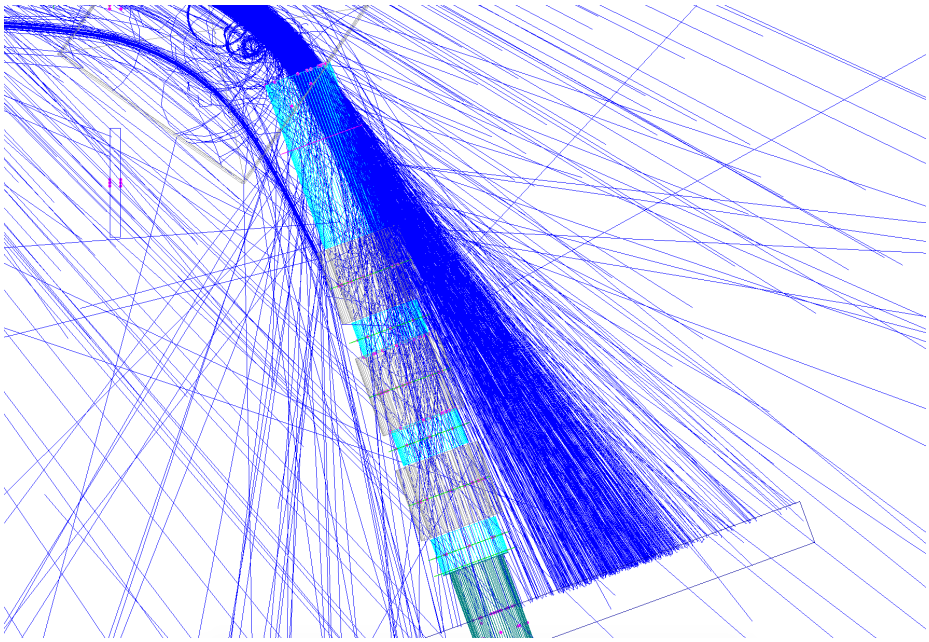

(a)

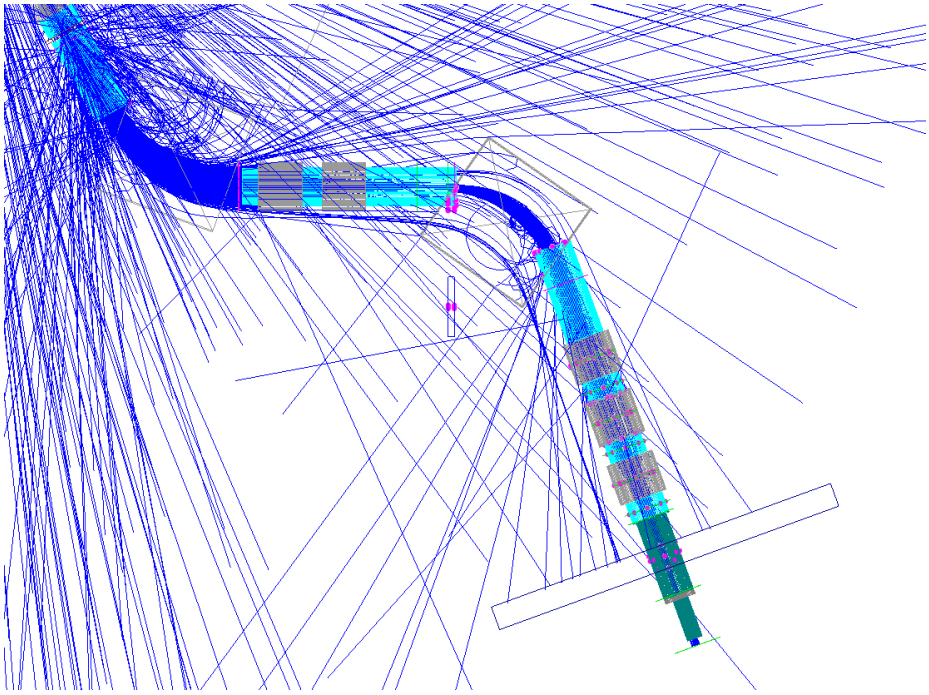

(b)

Figure 3.15: G4beamline 3D rendering of beamline for -13.3% tuning (b) and +9.9% tuning settings (a).

Chapter 4

Conclusion

In this study, an attempt was made to investigate the influence of various aspects of the `G4beamline` simulations on the M13 beamline. This was done in order to improve the confidence in the simulation's ability to accurately model the physical processes occurring within the beamline, and thus produce a final result on the proportion of low momentum positron events contributing to the tail in the crystal calibrator response function. After studying the effect of several initial beam distributions, electromagnetic fields and beamline components, it was determined that an appropriate upperlimit on the tail fraction from the beamline is 0.027 ± 0.0049 %. This proportion is significantly less than the 0.1% required for the precision of the experiment and confirms that the beamline does not contribute significantly to the overall tail correction calculations. Figure 4.1 shows this contribution of the beamline intrinsic tail fraction to the tail in the energy response.

Further study should include a finer analysis of the spatial deviation of the beam. This could be informed by obtaining information related to the emittance of the beam, if this information was obtained during data-taking. A more accurate determination of the starting distribution has significant implications on the final tail fraction, as established in Section 3.2.3.

Though it was intended for this work to include an analysis of the uncertainty in the reported beamline component locations, time constraints forbid this analysis. A determination of the upper and lower limit on these values would provide an systematic error on the tail fraction.

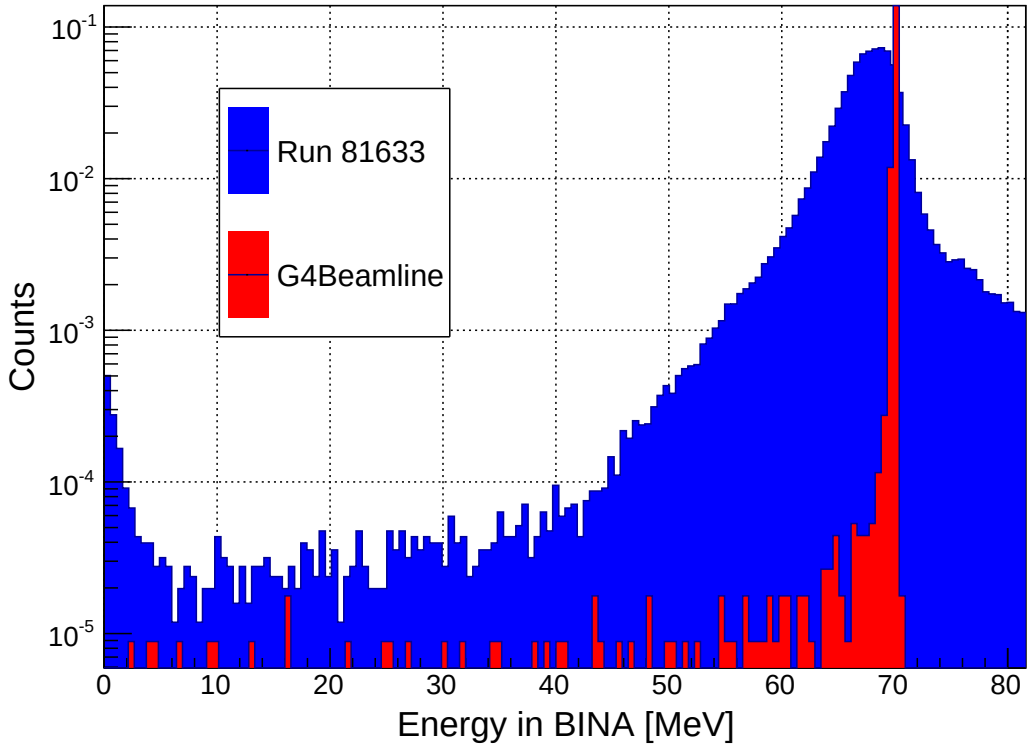

Figure 4.1: The contribution of the crystal calorimeter response tail (blue) that comes from the beamline (red) for the nominal case.

Bibliography

[1] Kazakov, D., Standard Model of Fundamental Interactions, Inspire HEP, 57, 2014. → pages vii, 2

[2] Thompson, M., Modern Particle Physics, Cambridge University Press, 554, 2013. → pages 1, 4

[3] K.A. Olive et al. (Particle Data Group), Chin. Phys. C38, 090001 (2014) (URL: http://pdg.lbl.gov) → pages v, 3

[4] Numao, T., Bryman D., Study of the decay $\pi \to e\nu$, TRIUMF Research Proposal, (2006). → pages 4

[5] Chlo Malbrunot et al 2011 J. Phys.: Conf. Ser. 312 102010. → pages 4

[6] Sullivan, T. A high-precision measurement of the $\pi \to e\nu$ branching ratio, University of British Columbia (PhD thesis), 2017. → pages vii, 4, 7

[7] A. Aguilar-Arevalo et al. (PIENU Collaboration), Improved Measurement of the the $\pi \to e\nu$ Branching Ratio, Phys. Rev. Lett. 115, 071801, 2015.. → pages 5

[8] K. A. Olive et al. Particle data group. Chin. Phys. C, 38, 2014 and 2015 update. doi:10.1088/1674-1137/38/9/090001. → pages 5

[9] Malbrunot, C., Study of $\pi \to e\nu$ decay, University of British Columbia, 2012. → pages vii, 7, 8, 11, 26

[10] Geant4 Collaboration, Geant4a simulation toolkit, Nuclear Instruments and Methods in Physics Research Section A: Accelerators, Spectrometers, Detectors and Associated Equipment, 2003 → pages 10

[11] Muons Internal, HistoRoot, 2014 → pages 11

[12] Walker, B., Momentum Distribution of a Parallel Positron Beam At F3, F4, PIENU Internal Documents (2007). → pages v, 13, 27

[13] Cuen, S., TN-30: MC for Positron Tail in M13beam-line, PIENU Internal Documents (2013). → pages viii, 14, 18

Appendix A

Relevant Scripts

A.0.1 merge.C

Merges the rotated beam `.root` files and overlays the run data from the BINA calorimeter.

```
{
#include "TFile.h"
#include "TMath.h"
#include "TNtuple.h"
#include "TCanvas.h"
#include "TStyle.h"
#include "TLegend.h"
#include "TImage.h"
#include "TGraph.h"

// plot the energy distribution of Cal.eBina
Int_t runNo = 81633;
Int_t numBins = 250;
Int_t start = 0;
Int_t stop = 1200;
Int_t canvasx = 800;
Int_t canvasy = 600;

gROOT->LoadMacro("/home/nrohan/449/analysis/scaleFunctions.C");

// 2012 data - Run 81633
char run[] = "/kdecay/data46/saulcuen/trees/beamline/...
tree081633_0_r422.root";
```

```
// Draw canvas
TCanvas *c1 = new TCanvas("c1","Simulation + Run Data",canvasx,canvasy);

// Histogram run data, normalize
TChain* tuple2012 = new TChain("T");
tuple2012->Add(run);
TH1F *h_BINA= new TH1F("h_BINA",Form("Cal.eBina for Run %d",runNo),...
numBins,start,stop);

//plot the run data
tuple2012->Draw("Cal.eBina>>h_BINA");

h_BINA->Draw("hist");
h_BINA->GetXaxis()->SetTitle("MeV");
h_BINA->SetTitle("BINA and Simulated Energy");
h_BINA->GetYaxis()->SetTitle("counts");
h_BINA->GetXaxis()->SetTitleSize(0.05);
h_BINA->GetYaxis()->SetTitleSize(0.05);
ScaleXaxis(h_BINA, ScaleX);
h_BINA->Draw();
h_BINA->ResetStats();
c1->SetGridy();
c1->SetGrid();
c1->SetFillColor(0);
c1->SetLogy();
c1->Update();

/*
A macro to merge g4beamline files
Files: angle0.1_0_0.root - angle0.1_320_360_run81633.root

*/

Int_t runNo = 81633;
Int_t numBins = 500;

Double_t xlow = -40.0;
Double_t xup = 40.0;

Float_t xcut = 40;
Float_t ycut = 40;
```

```
Float_t pxcut = 20;
Float_t pycut = 20;

Double_t plow = 0.0;
Double_t pup = 80.0;

TH1F *target_x = new TH1F("target_x", "", numBins, xlow, xup);
TH1F *target_y = new TH1F("target_y", "", numBins, xlow, xup);
TH1F *target_p = new TH1F("target_p", "", numBins, plow, pup);

for (int i = 0; i<9; i++){
        Int_t z_start = 40*i;
        Int_t z_stop = 40*(i+1);
        char *filename_to_add = Form("/kdecay/data46/nrohan/sim_run%d/...
    angle0.1_%d_%d_run81633.root", runNo, z_start, z_stop);
        cout << filename_to_add << endl;

        TFile *file_to_add = new TFile(filename_to_add, "READONLY");

        TNtuple *ntuple_to_merge = (TNtuple*) file_to_add->...
    Get("VirtualDetector/VD_F4");

        TH1F *temp_x = new TH1F("temp_x", "", numBins, xlow, xup);
        TH1F *temp_y = new TH1F("temp_y", "", numBins, xlow, xup);
        TH1F *temp_p = new TH1F("temp_p", "", numBins, plow, pup);

        // fill temp histograms
        ntuple_to_merge->Draw("x>>temp_x", Form("PDGid==-11 && ...
    abs(x)<%f && abs(y)<%f", xcut, ycut));

        ntuple_to_merge->Draw("y>>temp_y", Form("PDGid==-11 && ...
    abs(x)<%f && abs(y)<%f", xcut, ycut));

        ntuple_to_merge->Draw("sqrt(Px**2 + Py**2 + Pz**2)>>temp_p", ...
    Form("PDGid==-11 &&
    abs(x)<%f && abs(y)<%f", pxcut, pycut));

        // add to target
        target_x->Add(temp_x);
        target_y->Add(temp_y);
```

```
        target_p->Add(temp_p);

        delete file_to_add;
}
target_p->Draw("hist && sames");
c1->Update();
}
```

A.0.2 parseEPICS.py

Looks through `.ODS` files and prints the relevant information to put in `G4beamline`.

```
import sys
#f = open('/home/pienu/history/run816%s',30)
filename = ''
fileToWrite = open('FILE-TO-WRITE', 'w')
for rnum in range(30,72+1):
        filename = "/home/pienu/history/run816%s.odb" % (rnum)
        print(filename)
        try:
                f = open(filename,'r')
        except OSError:
                print("Cannot open file!")
        else:
                runNo = "run816%s" % (rnum)
                fileToWrite.write(runNo)
                fileToWrite.write("\n")
                for i, line in enumerate(f):
                        if line.find("[/Equipment/Epics/Settings]", 0, ...
            len(line)) != -1:
                                #store settings names into column 1
                                print(line, i)
                                #fileToWrite.write(line)
                        # if line.find("/Equipment/Epics/Variables]", ...
            0, len(line)):
                f.close
fileToWrite.close
```